The unprecedented 2017–2018 stratospheric smoke event:
Decay phase and aerosol properties observed with EARLINET

Holger Baars[1], Albert Ansmann[1], Kevin Ohneiser[1], Moritz Haarig[1], Ronny Engelmann[1], Dietrich Althausen[1], Ingrid Hanssen[2], Michael Gausa[2], Aleksander Pietruczuk[3], Artur Szkop[3], Iwona S. Stachlewska[4], Dongxiang Wang[4], Jens Reichardt[5], Annett Skupin[1], Ina Mattis[6], Thomas Trickl[7], Hannes Vogelmann[7], Francisco Navas-Guzmán[8], Alexander Haefele[8], Karen Acheson[9], Albert A. Ruth[9], Boyan Tatarov[10], Detlef Müller[10], Qiaoyun Hu[11], Thierry Podvin[11], Philippe Goloub[11], Igor Vesselovski[12], Christophe Pietras[13], Martial Haeffelin[13], Patrick Fréville[14], Michaël Sicard[15,16], Adolfo Comerón[15], Alfonso Javier Fernández García[17], Francisco Molero Menéndez[17], Carmen Córdoba-Jabonero[18], Juan Luis Guerrero-Rascado[19], Lucas Alados-Arboledas[19], Daniele Bortoli[20,21], Maria João Costa[20], Davide Dionisi[22], Gian Luigi Liberti[22], Xuan Wang[23], Alessia Sannino[24], Nikolaos Papagiannopoulos[25], Antonella Boselli[25], Lucia Mona[25], Giuseppe D'Amico[25], Salvatore Romano[26], Maria Rita Perrone[26], Livio Belegante[27], Doina Nicolae[27], Ivan Grigorov[28], Anna Gialitaki[29], Vassilis Amiridis[29], Ourania Soupiona[30], Alexandros Papayannis[30], Rodanthi-Elisaveth Mamouri[31], Argyro Nisantzi[31], Birgit Heese[1], Julian Hofer[1], Yoav Y. Schechner[32], Ulla Wandinger[1], and Gelsomina Pappalardo[25]

[1]Leibniz Institute for Tropospheric Research, Leipzig, Germany
[2]Andøya Space Center, Andenes, Norway
[3]Institute of Geophysics, Polish Academy of Sciences, Warsaw, Poland
[4]Faculty of Physics, University of Warsaw, Warsaw, Poland
[5]The Lindenberg Meteorological Observatory, Deutscher Wetterdienst, Tauche, Germany
[6]Meteorological Observatory Hohenpeissenberg, Deutscher Wetterdienst, Hohenpeissenberg, Germany
[7]IMK-IFU, Karlsruhe Institute of Technology, Garmisch-Partenkirchen, Germany
[8]Federal Office of Meteorology and Climatology, MeteoSwiss, Payerne, Switzerland
[9]Physics Department & Environmental Research Institute, University College Cork, Cork, Ireland
[10]School of Physics, Astronomy and Mathematics, University of Hertfordshire, Hatfield, United Kingdom
[11]LOA, Université de Lille, Lille, France
[12]Physics Instrumentation Center of General Physics Institute, Moscow, Russia
[13]Laboratoire Meteorologie Dinamique, École Polytechnique, Palaiseau, France
[14]Observatoire de Physique du Globe, Laboratoire de Météorologie Physique, Clermont-Ferrand, France
[15]CommSensLab, Dept. of Signal Theory and Communications, Universitat Politècnica de Catalunya, Barcelona, Spain
[16]CTE-CRAE/IEEC, Universitat Politècnica de Catalunya, Barcelona, Spain
[17]Centro de Investigaciones Energéticas, Medioambientales y Tecnológicas, Department of Environment, Madrid, Spain
[18]Instituto Nacional de Tècnica Aeroespacial, Atmospheric Research and Instrument. Branch, El Arenosillo/Huelva, Spain
[19]Andalusian Institute for Earth System Research and University of Granada, Granada, Spain
[20]Instituto Ciências da Terra, Universidade de Évora, Evora, Portugal
[21]Departamento de Física, Universidade de Évora, Evora, Portugal
[22]Consiglio Nazionale delle Ricerche, Istituto di Scienze Marine, Rome-Tor Vergata, Italy
[23]Consiglio Nazionale delle Ricerche, Istituto Superconduttori, Materiali Innovativi e Dispositivi, Naples, Italy
[24]Dipartimento di Fisica, Università degli studi di Napoli Federico II, Naples, Italy
[25]Consiglio Nazionale delle Ricerche, Istituto di Metodologie per l'Analisi Ambientale, Potenza, Italy
[26]Consorzio Nazionale Interuniversitario per le Scienze Fisiche della Materia e Università del Salento, Lecce, Italy

[27]National Institute of Research and Development for Optoelectronics, Magurele, Ilfov, Romania
[28]Institute of Electronics, Bulgarian Academy of Sciences, Sofia, Bulgaria
[29]IAASARS, National Observatory of Athens, Athens, Greece
[30]Laser Remote Sensing Unit (LRSU), Physics Department, National Technical University of Athens, Zografou, Greece
[31]Department of Civil Engineering and Geomatics, Cyprus University of Technology, Limassol, Cyprus
[32]Faculty of Electrical Engineering, Technion - Israel Institute of Technology, Haifa, Israel

Correspondence to: H. Baars
(baars@tropos.de)

Abstract. Six months of stratospheric aerosol observations with the European Aerosol Research Lidar Network (EARLINET) from August 2017 to January 2018 are presented. The decay phase of an unprecedented, record-breaking stratospheric perturbation caused by wild fire smoke is reported and discussed in terms of geometrical, optical, and microphysical aerosol properties. Enormous amounts of smoke (mainly soot particles) were injected into the upper troposphere and lower stratosphere over fire
5   areas in western Canada on 12 August 2017 during strong thunderstorm-pyrocumulonimbus activity. The stratospheric smoke plumes spread over the entire northern hemisphere in the following weeks and months. Twenty-eight European lidar stations from northern Norway to southern Portugal and the Eastern Mediterranean monitored the strong stratospheric perturbation on a continental scale. The main smoke layer (over central, western, southern, and eastern Europe) was found between 15 and 20 km height since September 2017 (about two weeks after entering the stratosphere). Thin layers of smoke were detected to
10   ascend to 22-24 km height. The stratospheric aerosol optical thickness at 532 nm decreased from values >0.25 on 21-23 August 2017 to 0.005-0.03 until 5-10 September, and was mainly 0.003-0.004 from October to December 2017, and thus still significantly above the stratospheric background (0.001-0.002). Stratospheric particle extinction coefficients (532 nm) were as high as 50-200 Mm^{-1} until the beginning of September and of the order of 1 Mm^{-1} (0.5-5 Mm^{-1}) from October 2017 until the end of January 2018. The corresponding layer mean particle mass concentration was of the order of 0.05-0.5 $\mu g\ cm^{-3}$
15   over the months. Soot is an efficient ice-nucleating particle (INP) at upper tropospheric (cirrus) temperatures and available to influence cirrus formation when entering the tropopause from above. We estimated INP concentrations of 50-500 L^{-1} until the first days in September and afterwards 5-50 L^{-1} until the end of the year 2018 in the lower stratosphere for typical cirrus formation temperatures of $-55°C$ and ice supersaturation values of 1.15. The measured profiles of the particle linear depolarization rato indicated the predominance of non-spherical soot particles. The 532 nm depolarization ratio decreased with time
20   in the main smoke layer from values of 0.15–0.25 (August-September) to values of 0.05–0.10 (October-November) and <0.05 (December-January). The decrease of the depolarization ratio is consistent with the steady removal of the larger smoke particles by gravitational settling and changes in the particle shape with time towards a spherical form. An ascending layer with a vertical depth of 500-1000 m was detected (over the Eastern Mediterranean at 32-35°N) that ascended from about 18-19 km to 22-23 km height from the beginning of October to the beginning of December 2017 (about 2 km per month) and may be
25   related to the increasing build up of the winter-hemispheric Brewer-Dobson circulation system.

1 Introduction

Record-breaking wildfire activity in British Columbia during the summer of 2017 coupled with rather favorable weather conditions on 12 August 2017 triggered the evolution of five major thunderstorms over western Canada in the afternoon of this day (Peterson et al., 2018). Exceptionally strong and well organized pyrocumulonimbus (pyroCb) clusters (Fromm et al., 2010;

5 Peterson et al., 2017) developed over the fire areas and lifted enormous amounts of fire smoke into the upper troposphere and lower stratosphere (UTLS) (Khaykin et al., 2018; Peterson et al., 2018; Ansmann et al., 2018; Hu et al., 2019). Within pyroCbs the upward transport takes usually less than one hour from the ground to the tropopause level (Fromm et al., 2000, 2003; Rosenfeld et al., 2007). Many of the smoke particles may have served as cloud condensation nuclei (CCN) and ice-nucleating particles (INP), but the amount of smoke particles was so large that most of them were just lifted as interstitial aerosol to the

10 UTLS region. The particles obviously reached the stratosphere as pure soot particles without any significant interaction with gaseous constituents as multiwavelength polarization lidar observations suggest (Haarig et al., 2018; Hu et al., 2019). Self-lifting effects (Boers et al., 2010; Siddaway and Petelina, 2011; de Laat et al., 2012) then lead to a further significant ascent of the soot-containing layers. The aerosol optical thickness (AOT) in the UTLS region must have exceeded values of 2–3 at 500 nm wavelength so that strong absorption of sunlight occurred and enabled the smoke layers to ascend by about 2-3 km per

15 day during the first days after injection as was observed with the spaceborne lidar aboard CALIPSO (Cloud-Aerosol Lidar and Infrared Pathfinder Satellite Observation) (Khaykin et al., 2018).

Peterson et al. (2018) discussed the strength of this stratospheric smoke event based on spaceborne lidar observations and passive remote sensing and concluded that the pyroCb driven aerosol injection into the UTLS was comparably with a moderate volcanic eruption characterized by a Volcanic Explosivity Index of 3-4. The 12 August 2017 event, denoted as Pacific Northwest

20 Event by Peterson et al. (2018), injected 0.1-0.3 Tg of total aerosol particle mass into the lower stratosphere. However, such mass comparisons do not provide an adequate description of the difference regarding the impact on atmospheric processes. Volcanic and smoke particles show rather different chemical, physical and morphological properties. In contrast to liquid, spherical, less light-absorbing sulfuric acid droplets of volcanic origin, stratospheric soot particles from the wildfires in 2017 were observed to be non-spherical (Haarig et al., 2018; Hu et al., 2019), and thus solid (even with no liquid shell). They can

25 significantly absorb solar radiation (Boers et al., 2010). Soot particles influence the evolution of cirrus clouds by serving as INP in heterogeneous ice nucleation processes (Hoose and Möhler, 2012; Kanji et al., 2017; Ullrich et al., 2017), in contrast to liquid sulfuric acid droplets which influence cirrus occurrence and evolution via homogeneous ice nucleation (Jensen and Toon, 1992; Sassen et al., 1995; Liu and Penner, 2002).

After injection on 12 August 2012, the smoke traveled to northern Canada, and then through the jet stream eastward, crossed

30 the North Atlantic and reached Europe on 21-23 August 2017 (Ansmann et al., 2018; Haarig et al., 2018; Zuev et al., 2019; Hu et al., 2019). Compared to the maximum stratospheric perturbation over Europe after the eruption of Mt. Pinatubo in 1991 (Ansmann et al., 1997), 20 times higher particle extinction coefficients were observed in the lower stratosphere over Germany on 22 August 2017 (Ansmann et al., 2018). The smoke spread over the entire northern hemisphere during the following weeks, mostly at heights below 20 km with the dominating westerly air flow, and reached even the tropics via the dynamical transport

around the Asian monsoon anticyclone (Kloss et al., 2019). The strong stratospheric perturbation diminished slowly from September 2017 to May-June 2018 according to SAGE III-ISS (Stratospheric Aerosol and Gas Experiment III mounted aboard the International Space Station) and OMPS-LP (Ozone Mapping Profiler Suite Limb Profiler onboard Suomi National Polar-orbiting Partnership, Suomi NPP) observations (Kloss et al., 2019). Part of the smoke particles ascended to heights of 20-25 km

5 and enriched the natural soot particle reservoir located between 20 and 30 km height (Renard et al., 2008). The stratospheric smoke influenced radiative transfer (Ditas et al., 2018; Kloss et al., 2019), chemical processes, and probably cirrus evolution after entering the upper troposphere via gravitational settling and other processes causing an effective downward transport.

This historical event of a strong and long-lasting stratospheric aerosol perturbation was observed all over Europe with ground-based lidar systems of the European Aerosol Research Lidar Network (EARLINET) (Pappalardo et al., 2014). The

10 arrival of first optically dense smoke plumes and layers over France was documented by Khaykin et al. (2018) and Hu et al. (2019) and over Central Europe in the accompanying articles of Ansmann et al. (2018) and Haarig et al. (2018). As a highlight, the smoke particles could be characterized regarding size distribution and shape properties at Leipzig (Germany) and Lille (France) by means of triple-wavelength polarization lidar observations (Haarig et al., 2018; Hu et al., 2019).

In this study, we present the observations from August 2017 to the end of January 2018 and discuss the decay phase and

15 the changing optical and microphysical properties of the smoke particles over the almost six-month period. A strong role in the long-lasting 2017-2018 monitoring effort played the subnet PollyNET (NETwork of POrtabLe Lidar sYstems) (Baars et al., 2016) which consists of continuously running multiwavelength polarization/Raman lidars. The smoke layers were well detectable even six months after the injection until the end of January 2018. We will discuss the stratospheric perturbation in terms of layer base and top heights, AOT and column mass load, vertically mean extinction coefficients and soot mass

20 concentrations, and even in terms of INP concentration estimates.

Note that the first lidar network observations of a pyroCb-related stratospheric smoke event was presented by Fromm et al. (2008) after the Chisholm Fire event in May 2001. Six lidar stations at Ny Ålesund on Spitsbergen, at Esrange, Sweden, the EARLINET sites of Kühlungsborn and Garmisch-Partenkirchen, Germany, at Boulder, Colorado, and Mauna Loa, Hawaii, observed the meridional spread of smoke from 20°N to 79° within one month. Smoke features persisted on a hemispheric scale

25 for at least 3 months. The German EARLINET station of Garmisch-Partenkirchen has also one of the longest stratospheric aerosol records in the world (Trickl et al., 2013). The effects of major volcanic eruptions (El Chichon, Pinatubo) and numerous moderate volcanic eruptions are documented at Garmisch-Partenkirchen in southern Germany since 1976 . Also longer periods of quiescent times (to determine minimum stratopsheric aerosol background levels) are included in the almost 40-year data record.

30 ## 2 Lidar networks: EARLINET and PollyNET

Twenty-three EARLINET stations from northern Norway (at 69°N) to Cyprus (34.5°N) (Pappalardo et al., 2014) contributed to the study. The lidar stations are shown in Fig. 1 together with five additional non-EARLINET lidar stations at Hatfield (UK), Lindenberg (Germany), El Arenosillo (Spain), Kosetice (Czech Republic), and Haifa (Israel). These non-EARLINET stations

are closely collaborating with the EARLINET team under the umbrella of the European infrastructure project ACTRIS-2 (Aerosols, Clouds, and Trace gases Research InfraStructure, https://www.actris.eu/) which is a pan-European initiative consolidating actions amongst European partners producing high-quality observations of aerosols, clouds and trace gases. ACTRIS is composed of observing stations, exploratory platforms, instrument calibration centers, and a data center, and aims to sup-

5 port atmospheric and environmental science by providing a platform for researchers to combine their efforts more effectively. Different lidar systems are operated at the EARLINET stations but the quality assurance / quality control (QA/QC) programs developed and run within ACTRIS RI (research infrastructure) allow a continuous control of the lidar operation and data. Among the considered 28 stations, there are seven continuously measuring Polly instruments (Althausen et al., 2009; Engelmann et al., 2016; Baars et al., 2016) operated at Kosetice, Limassol (Cyprus), Haifa, Warsaw (Poland), Hohenpeissenberg

10 (Germany), Evora (Portugal) and at Finokalia on Crete (Greece).

  Most of the EARLINET aerosol lidars are not designed for stratospheric aerosol observations. They are optimized for tropospheric measurements (boundary layer aerosols, diurnal cycle of PBL conditions, lofted dust plumes in the free troposphere). The Polly instruments have, e.g., a 30 cm telescope and a small laser emitting light pulses of 110 mJ at 532 nm at a repetition rate of 20 Hz. In contrast, the big Leipzig EARLINET lidar (Mattis et al., 2010; Haarig et al., 2018; Jimenez et al., 2019) has

15 an 80 cm telescope, 500 mJ per laser pulse at 532 nm and a repetition rate of 30 Hz. This lidar is highly capable to monitor stratospheric aerosol even at background conditions (Mattis et al., 2010; Finger, 2011). Most measurements presented in Sect. 3 are performed with the Polly instruments. Long averaging times (of typically 3-6 hours during nighttime hours) and vertical smoothing lengths of several 100 m had to be applied in the data analysis. An example is shown in Fig. 2. Fortunately, aerosol layering structures in the stratosphere are usually long-lasting, coherent, and persistent over many hours and sometimes even

20 over days so that long temporal averaging and signal smoothing will not remove essential information about the observed stratospheric smoke layers.

  In Sect. 3, quality-assured lidar observations are presented and discussed, mostly based on the retrieval of particle backscatter coefficients and particle linear depolarization ratio at 532 nm. Details of the lidar data analysis can be found in D'Amico et al. (2015, 2016); Mattis et al. (2016); Freudenthaler (2016); Baars et al. (2016); Mamouri and Ansmann (2016, 2017). The

25 EARLINET observations are taken from the EARLINET data base (EARLINET, 2019) and selected by careful inspection of the involved lidar teams. The Polly data analysis were performed by following the EARLINET data analysis protocols and procedures. To compute and correct for molecular backscatter and extinction contributions to the lidar backscatter signals, GDAS (Global Data Assimilation System) air temperature and pressure data were partly used in the Polly data analysis (GDAS, 2019). However, most days were analyzed by assuming standard atmospheric conditions in the stratosphere. Significant differences to

30 the results obtained with GDAS data were not observed.

  Except the Lindenberg and Payerne (Switzerland) lidars, all participating stations provided height profiles of the particle backscatter coefficient β_{p} at 532 nm. Several stations could successfully measure the 532 nm volume (i.e., Rayleigh + particle) linear depolarization ratio and the respective particle depolarization ratio in the stratosphere. The powerful lidar system of the Meteorological Observatory Lindenberg of the German Weather Service provided the optical properties at 355 nm. The

35 height profiles of the particle backscatter coefficient were used to determine base height z_{bot} and top height z_{top} of the de-

tected stratospheric smoke layers and. In the next step, the layer mean and column-integrated smoke optical properties were calculated.

The relative uncertainties in the lidar products shown in Sect. 3 are of the order of 10-30% (particle backscatter coefficients), 20-50% (particle extinction estimates and AOT estimates), and 10-30% for the presented smoke layer mean values for the

5   particle depolarization ratio. The smoke layer geometrical properties (base and top heights) may have an uncertainty of the order of 50-150 m. The larger uncertainties describe the data quality for the observational period from October 2017 to January 2018. Signal noise is the main contributor to the large uncertainties.

Figure 2 presents an example of a complete Polly data analysis. A stratospheric smoke observation taken at Limassol, Cyprus, from 18:00–24:00 UTC on 9 September 2017 is shown. Height-time displays of the range-corrected signals indicated almost

10   constant backscatter conditions over the six-hour period. The six-hour mean lidar return signals were vertically smoothed with a gliding averaging window length of 367.5 m before the calculation of the particle optical properties as a function of height above sea level (a.s.l.). The volume linear depolarization ratio at 532 nm in Fig. 2a, simply obtained from the calibrated cross-to co-polarized signal ratio, enabled us to unambiguously identify the smoke layer in most cases. By means of the profiles of the volume depolarization ratio and the particle backscatter coefficient (in Fig. 2b) the particle linear depolarization ratio δ_p at

15   532 nm in Fig. 2c was calculated. The indicated base and top heights, z_{bot} and z_{top}, of the smoke layer are the mean values obtained from several 60-90-minute mean backscatter profiles measured from 18:00-24:00 UTC.

Based on the profiles in Fig. 2, layer mean values of the particle backscatter coefficient $\overline{\beta_p}$ and particle linear depolarization ratio $\overline{\delta_p}$ were computed (as given in Fig. 2). By assuming an appropriate smoke extinction-to-backscatter ratio (lidar ratio) of 65 sr at 532 nm (Haarig et al., 2018), we obtained the aerosol optical thickness (AOT) τ_p and the layer mean particle extinction

20   coefficient $\overline{\sigma_p}$ also given in Figure 2. The relative uncertainties in the layer mean optical properties are of the order of 20-50%. An overview of all lidar products together with the needed input parameter assumptions is given in Table 1. The listed input parameters were used throughout the investigated period from August 2017 to January 2018 and applied to all EARLINET data shown below.

By means of the computed optical properties, the microphysical properties, i.e., the soot mass concentration M_p and the ice-

25   nucleating particle concentration n_{INP} were estimated. Here, conversion factors such as the soot particle extinction-to-volume conversion factor c_v and extinction-to-surface conversion factor c_s (Mamouri and Ansmann, 2016, 2017), the density ρ_p of the soot particles or the mass-specific extinction coefficient k_{ext} are required. From the measured smoke optical properties and the derived microphysical properties (from multiwavelength lidar inversions), presented by Haarig et al. (2018) for the optically dense smoke layer observed over Leipzig, Germany on 22 August 2017, the extinction-to-volume and extinction-to-

30   surface conversion factors c_v and c_s in Table 1 were obtained. The soot particle density is highly variable and can vary from 0.2–2 $\mu g\ cm^{-3}$ (Rissler et al., 2013). As a compromise, we selected arbitrarily a value of 0.9 $\mu g\ cm^{-3}$ in our study. Similarly, the mass-specific extinction coefficient can vary from about 3 $m^2\ g^{-1}$ to >15 $m^2\ g^{-1}$ (Smith et al., 2015; Forestieri et al., 2018). Thus, the mass concentration estimation is highly uncertain (factor of 2-3). The INP concentration n_{INP} (see Table 1) is computed by using an INP parameterization developed for heterogeneous ice nucleation on soot particles via deposition

35   nucleation (i.e., direct deposition of water vapor on the INPs) (Ullrich et al., 2017). Input aerosol parameter is the particle

surface area s_p. In addition, the atmospheric conditions (ambient temperature T and ice supersaturation S_ice within the cirrus layer) are considered in the n_INP calculation via the η_dep term (see Table 1). The INP efficacy of aerosol particles increases by an order of magnitude when the temperature decreases by 5 K and is thus highest at tropopause level (coldest point of the troposphere). This behavior is described by the η_dep term (Mamouri and Ansmann, 2016; Ullrich et al., 2017). The relative

5 uncertainty of the entire INP retrieval is determined by the large uncertainty (factor of 2-5) in the INP parameterization (Ullrich et al., 2017).

3   Observations

3.1   Decay of the stratospheric perturbation

Figure 3 provides an overview of the stratospheric smoke observations conducted with the 28 lidar systems. We considered all
10 observations above 10 km height (a.s.l.) during the first four weeks after injection (until 9 September 2017). Afterwards (since 10 September), only the layers clearly above the local tropopause are shown. Vertical lines represent individual observations (one per day and site) of the detected smoke layers from base to top. The observations were taken after sunset and signal averaging time periods were at least 2 hours, with only a few exceptions. We subdivided the EARLINET observations according to the colors used in Fig. 1 for northern Europe (black, Norway), central and western Europe (green), the Iberian peninsula
15 (blue, Spain and Portugal) and for southeastern Europe (red, mainly central and eastern Mediterranean stations). Most of the Polly observations will be presented in Fig. 4 and are given here as grey background lines.

Smoke was frequently detected all over Europe until the end of October 2017 as the dense set of colored vertical lines indicate. Within a few weeks, the smoke obviously spread over large parts of the northern hemisphere. This is corroborated by the lidar observations aboard the CALIPSO satellite (Kar et al., 2019) in August and September 2017. The same behavior
20 was also reported by Fromm et al. (2008) after the Chisholm pyroCB-related stratospheric smoke event in 2001. In northern Norway (69°N), the 2017 smoke layer was observed below 16 km height (because of the low tropopause height), whereas over the central, western and southern European stations, the smoke reached to 22 km height. Also the spaceborne lidar shows this height dependence in terms of latitudinally resolved zonal averages of the attenuated total-to-Rayleigh backscatter ratio (Kar et al., 2019). According to the ground-based lidar observations in Fig. 3 the layer depth was frequently 1-2.5 km and in
25 some cases even more than 5 km. Sicard et al. (2019) investigated the dispersion of the smoke which arrived over the Iberian Peninsula on 7-8 September 2017 in detail based on the Portuguese and Spanish lidar observations (the SW European lidar team in our study here, indicated by blue lines in Fig. 3) and spaceborne lidar observations aboard CALIPSO.

The Polly observations in Fig. 4a collected at Evora (Portugal), the central European stations of Hohenpeissenberg (Germany) and Kosetice (Czech Republic), and in the Eastern Mediterranean (Limassol, Haifa) show that the layer top frequently
30 exceeded 20 km since mid September 2017 until the end of the year. The main smoke layer was found between 15 and 20 km height. The smoke was frequently detected over southwestern and central Europe in the beginning of the smoke period (August-September 2017), and then mostly over the Eastern Mediterranean (October 2017 to January 2018). The data analysis was stopped at the end of January 2018 because no significant smoke layer was found anymore over Limassol and Haifa during

the following months. The results are again in agreement with the spaceborne lidar observations of the zonally averaged smoke optical properties and the detected latitudinal differences regarding occurrence, height, and vertical depth of the smoke layers in the months from September to November 2017 (Kar et al., 2019).

As shown in Fig. 4b, the stratospheric AOT at 532 nm decreased rapidly from values >0.2 in August 2017 to values between 0.005 and 0.03 in the beginning of September 2017, and afterwards the AOT ranged from 0.002 (almost stratospheric background conditions) to 0.008 with most values between 0.003 and 0.004 (over Limassol and Haifa, mid September to December 2017). A lidar ratio of 65 sr was applied to the respective column-integrated particle backscatter coefficients, integrated over the vertical column from z_{bot} to z_{top} (see Fig. 2), to obtain the AOT values. The AOT fluctuations are partly caused by the relatively strong impact of signal noise on the retrieval results. However, also atmospheric variability contributed to the observed fluctuations and to the respective vertically mean extinction coefficients (mean backscatter coefficient for the vertical column from z_{bot} to z_{top} multiplied with the soot lidar ratio of 65 sr) shown in Fig. 4c. We observed vertically mean 532 nm particle extinction coefficients for the smoke layers from 10-200 Mm^{-1} in August 2017, 2-50 Mm^{-1} until 5 September 2017, 1-10 Mm^{-1} until the end of September, and finally values from 0.5-5 Mm^{-1} (accumulating around 1 Mm^{-1}) until the end of January 2018.

532 nm AOT values around 0.004 indicate already typical stratospheric aerosol conditions for periods without major volcanic eruptions as discussed in Trickl et al. (2013) and in further articles reviewed and summarized in Ansmann et al. (2018). Based on 731 clear sky EARLINET nighttime lidar observations at Leipzig from January 2000 to June 2008 we conclude, however, that the minimum stratospheric AOT is of the order of 0.001 to 0.002 for the layer from 1 km above the tropopause to the top of the identified aerosol structures (<30 km height) (Finger, 2011). This is in accordance with the long-term observations presented by Trickl et al. (2013) and spaceborne stratospheric background observations presented by Kloss et al. (2019) and Vernier et al. (2018). When using a typical extinction-to-backscatter ratio of 50 sr (for non-soot particles), the vertically mean particle extinction coefficients at minimum stratospheric aerosol conditions are in the range of 0.1–0.2 Mm^{-1} at 532 nm (Finger, 2011).

We compared our findings with measurements of the particle extinction coefficient at 521 nm wavelength aboard the International Space Station (ISS, SAGE III) presented by Kloss et al. (2019). For the more homogeneous period from October to December 2017, they found the main smoke layer also between 15 and 20 km height. Kloss et al. (2019) analyzed stratospheric extinction measurements for an area from 25–38°N and 40-95°E (covering the Middle East, Central Asia, and western China). The Polly stations at Cyprus and Israel were just west of this data analysis region. The mean extinction coefficients for this large area of almost 1000 km × 5000 km were about 0.5-1 Mm^{-1} during the October-December period, and hence in good agreement with the Polly observations. The good agreement also indicates that the assumed smoke lidar ratio of 65 sr at 532 nm is justified. For the entire northern hemisphere (>40°N), Kloss et al. (2019) found mean particle extinction coefficients of 0.8-1 Mm^{-1} for the October-December period and for the height range from about 14-19 km. According to the SAGE III and OMPS-LP observations stratospheric background extinction values were again reached in April-May 2018, about 8–9 months after the intense smoke injection event.

After conversion of the smoke extinction coefficients into respective mass concentrations (see Sect. 2 for more details) we found smoke mass concentrations of the order of 1–25μg cm^{-3} in August and the beginning of September (see Fig. 4c), and afterwards frequently values from 0.1–1 μg cm^{-3}. Minimum stratospheric background values are <0.02 μg cm^{-3} (Finger, 2011). Column mass concentrations exceeded 10 mg m^{-2} in August 2017, and later on most values were found in the range from 0.1–1 mg m^{-2} (see Fig. 4b). The particle mass estimates are uncertain by a factor of 2-3 due to the unknown soot particle density.

Figure 5 highlights the potential of soot particles to serve as INP and to discuss the potential impact on ice formation at tropopause level. The extinction coefficients in Fig. 4c were converted to INP concentrations for a typical cirrus formation temperature of $-55°$C and typical supersaturation conditions expressed by $S_{ice} = 1.15$. Besides slow downward motion by gravitational settling of the soot particles, an efficient way to transport aerosol from the lower stratosphere downward to the upper troposphere are stratospheric intrusions (Trickl et al., 2014, 2016). Smoke particles reaching the upper troposphere and entrained into ascending humid tropospheric air masses may trigger cirrus formation at conditions with ice supersaturation values <1.4, still not favorable for homogeneous ice nucleation which needs ice supersaturation levels of typically 1.5-1.7. Heterogeneous ice formation on soot particles may thus have slightly enhanced cirrus formation in the northern hemisphere, especially during the first few months after injection.

The observed smoke extinction coefficients indicate INP concentrations of 3000 L^{-1} in the beginning of the event during August 2017, then 50-500 L^{-1} until 5 September, 10-300 L^{-1} until 20 September, 5-50 L^{-1} until November, and finally <20 L^{-1} until the end of January 2018 for $T = -55°$C and $S_{ice} = 1.15$. These values are large and can sensitively disturb cirrus formation in the usually clean upper troposphere.

3.2 Particle shape and size characteristics

Haarig et al. (2018) and Hu et al. (2019) discussed the shape properties of the soot particles injected into the dry stratospheric environment. In the introdcution section, it was mentioned that the vertical transport from the surface to the tropopause within pyrocumulonimbus towers may have lasted less than an hour and that probably most of the smoke particles were just lifted as interstitual aerosol (i.e., non-activated particles which did not serve as cloud condensation nuclei or ice-nucleating particles). In the dry stratosphere, any remaining water or liquid shell around the solid soot particles was probably removed according to the studies of the three-wavelength depolarization-ratio studies of Haarig et al. (2018) and Hu et al. (2019). Spherical particles, e.g., soot particle cores with a liquid sulfate shell (Dahlkötter et al., 2014), produce small particle linear depolarization ratios (0-0.03). In contrast, the non-spherical soot particles observed in August 2017 caused high particle linear depolarization ratios, most frequently of 0.2–0.25 and 0.15–0.2 at 355 and 532 nm, respectively, and low depolarization ratio of 0.03–0.07 at 1064 nm. Haarig et al. (2018) concluded that this strong wavelength dependence of the depolarization ratio reflects the specific characteristics of the size distribution of the smoke particles. A monomodal aged accumulation mode was derived by means of inversion of the multiwavelength lidar data measured on 22 August 2017. A well-developed coarse mode was completely absent. The particles had diameters from 400 to 1400 nm with the mode maximum at 600-700 nm. Based on the multiwavelength lidar observation of the lidar ratio and depolarization ratio by Haarig et al. (2018), an extensive simulation

study of the optical properties of the non-spherical smoke particles has been performed (Gialitaki et al., 2019). This study suggest that the smoke particles were compact and almost spherical in shape.

In Fig. 6, we provide an overview of all available 532 nm depolarization ratios measured with the ACTRIS/EARLINET lidar consortium from August 2017 to the end of January 2018. A few 355 nm particle depolarization values are included (Lindenberg). Most values are contributed by the Polly lidars. In the beginning, orange and red colors prevailed. The retrieved particle depolarization ratios were between 0.15–0.25. Because the tropospheric lidars were not optimized for stratospheric observations (at relatively low backscatter and AOT conditions), a significant contribution of signal noise to the variability in the depolarization ratio values has to be considered. However, a general trend, i.e., a decrease of the depolarization ratio with time towards 0.05–0.1 and later <0.05 is clearly visible. This decrease of the layer mean depolarization ratio is probably partly caused by the removal of the larger smoke particles. The smaller the remaining smoke particles the lower the depolarization ratio. This size dependence was already discussed in Mamouri and Ansmann (2014, 2017) for mineral dust and in Haarig et al. (2018) for the smoke particles. The second option is that the particles changed their shape from a non-spherical towards a spherical form. The soot particles may have interacted with gaseous components in the stratosphere over the months with the result that a spherical shell formed around the solid soot cores.

In Fig. 4a, we see a coherent, apparently upward moving structure of typically <1000 m vertical extent. It seems that this layer appeared already in September over Portugal (blue, Evora observations) and then more clearly and frequently over the Eastern Mediterranean (red, Limassol, orange, Haifa). In Fig. 7, this ascending smoke branch is separated from the main smoke layer which is shown in Fig. 8. In a few cases, we were able to determine the depolarization ratio within the thin layer and concluded from the slightly larger values (compared to the ones in the main layer) that the particles in the upward moving layer were on average a bit larger in size than the ones in the main smoke layer between 15 and 20 km height. A strong difference in the aerosol and depolarization features, keeping the large impact of signal noise on the result into account, is however not found. Also the vertically averaged (layer mean) extinction coefficients were similar in the two layers and indicated similar smoke conditions in both layers (see Figs. 7b and 8b).

At the end of this section, Fig. 9 provides a statistical overview of the smoke layer depths. The 435 daily Polly observations (conducted after sunset from August 2017 to January 2018) in Fig. 9a illustrate that the vertical depth of the smoke layers was between 500 and 1500 m in 50% of all cases. However, smoke layer depths of several kilometers were also observed. The ascending layer showed a more narrow distribution of layer depths. They were frequently between 500 and 1000 m. Figure 9c shows the full variability of layer depths for the main smoke layer during the long-range transport phase (October 2017 to January 2018) based on the Polly observations at Evora, Hohenpeissenberg, Kosetice, Limassol, and Haifa.

3.3 Underlying transport processes

Figures 3, 4, and 6-8 allow us to discuss the underlying aerosol transport processes and the reason for the observed apparent upward movement of one of the smoke features (i.e., for the apparent cross adiabatic flow). The main stratospheric smoke layer in Figs. 6 and 8a is the result of the permanently occuring stratospheric west-to-east transport with the prevailing westerly winds (jet stream). A descending trend (downward moving of the layer) is not visible from September 2017 to January 2018

in this layer. Gravitational settling and warming of the air mass by absorption of solar radiation by the soot particles may have compensated each other. However, the decrease of the depolarization ratio is consistent with a change of the size distribution towards smaller particles as well as with a change in particle shape as mentioned already.

The most interesting question is: Can we explain the steady upward movement (over months) of the ascending layer in
5 Fig. 7a? The layer ascended from about 18-20 km in mid October to 22-23 km in the beginning of December 2017 (layer at 22-23 km height). The apparent ascent velocity was about 70 m per day or 2 km per month. If we include the Evora Polly observations (September data in Fig. 7), the layer ascended from 16 km (10 September 2017) to 23 km (5 December 2017), and thus about 7 km in 85 days or 80 m per day.

Three smoke lifting processes are discussed in the literature. The first one is related to the gravito-photophoresis effect
10 (Rohatschek, 1996; Pueschel et al., 2000; Cheremisin et al., 2005, 2011). Upward motion of individual particles is caused by radiometric forces resulting from normal stresses on the particle surface due to temperature gradients in the gas surrounding the surface (i.e., by temperature differences between the particle surface and the surrounding gas). Gas molecules continuously impact on the surface of an aerosol particle and are reflected (Cheremisin et al., 2011). During reflection the molecules may pick up some energy and leave the surface with a higher thermal energy. The required temperature gradients are produced by
15 a difference in the thermal accomodation coefficient (in case of particle lifting the accomodation coefficient at the bottom of the particle is higher than at its top). The sun is the source of irradiance and negative photophoresis takes place, that is, a force pointing to the sun poses a lifting component that opposes the forces of gravity (Rohatschek, 1996; Pueschel et al., 2000). Very specific aerosol and atmospheric conditions must be fulfilled. Only particles well-aligned in the air flow can be lifted. Stable alignment (and lifting) is only possible in the case of larger particles for which the center of gravity is then always below their
20 geometrical center (i.e., in the lower half of the particles during lifting). However, if particles are too large and thus too heavy, gravitational settling will always dominate. Optimum sizes (diameters) of particles for lifting are 1-2 μm. A stable equilibrium with the force of gravity pointing to the Earth and the photophoretic force pointing upward will build up for these particles. However, as shown by Pueschel et al. (2000) for irregularly shaped stratospheric soot particles (chains of spherules) with sizes or lengths of 1 μm the resulting vertical velocity is 0.009 cm/s or about 7-8 m per day at heights around 20 km. Thus the
25 gravito-photophoresis effect cannot explain the found strong upward movement of the order of 70-80 m per day. Furthermore, this effect is active in both layers, the main layer in Fig. 8 and in the ascending layer in Fig. 7.

The second process leading to a cross adiabatic movement (by diabatic heating) is related to the so-called self-lifting effect (Boers et al., 2010; Siddaway and Petelina, 2011; de Laat et al., 2012). Absorption of shortwave solar radiation heats the smoke layers and creates buoancy that can then result in an ascent of the aerosol layer over several kilometers altitude within 1-2 days
30 (Siddaway and Petelina, 2011; de Laat et al., 2012). Such a heating is seasonally dependent. The largest lifting effect occurs in the summer hemisphere around 21 June when aerosol layers are exposed to sunshine for close to 24 hours a day. Boers et al. (2010) demonstrated in the case of soot (assuming a single scattering albedo of 0.75 at 500 nm) for mid summer conditions at 40°N (approximately for Evora, Limassol, and Haifa in late summer) that an ascent rate of 2.5 km per day is possible in the case of a smoke AOT of 3.5 (at 500 nm). For an AOT of 0.5, lifting is of the order of 400-500 m per day, and for an AOT of
35 0.003-0.005, a lifting velocity of a few meters per day during mid summer conditions is plausible. However, the strong lifting

over Limassol and Haifa was observed in autumn (from October to December). In conclusion, the self-lifting effect can also be ruled out as an explanation for the measured upward movement of one of the smoke layers. Again, this effect is active in both layers.

The third process that can cause upward motion of smoke is the Brewer-Dobson circulation (BDC) (Butchart, 2014; Seviour et al., 2012). Kloss et al. (2019) showed for the 2017 Canadian smoke event (based on comprehensive atmospheric modeling and spaceborne smoke observations) that the transport of fire smoke from higher to lower northern hemispheric latitudes in August and September 2017 was mediated by the Asian summer monsoon anticyclone (AMA, active until the end of September). A substantial part of the wildfire-based smoke plume was entrained into the anticyclonic flow at the AMA boundaries in the UTLS region and was then transported towards the tropics. In the tropics, the smoke layers were lifted by about 1.5 km per month in the upwelling branch of the BDC (Kloss et al., 2019) and then transported northward in accordance with the meridional Brewer-Dobson circulation. During the October-December period the BDC is in the winter-mode build-up phase. A steady lifting of the smoke layers in the tropics of 50-100 m per day (over several months) as part of BDC and the subsequent northward transport of the lifted layers can thus produce an apparently ascending smoke feature as observed over Limassol (34.5°N) and Haifa (32.5°N). The later in the year the northward transport starts the higher the layer could be lifted before. The two different, independent layers (one circulating around the globe with the strong westerly winds in Fig. 8, and another arriving from the tropics and influenced by the BDC) merged outside the tropics.

Our hypothesis of a BDC impact is corroborated by smoke observations from the summer of 2017 to the summer of 2018 (SAGE III observations, mean extinction coefficients for an area over Asia, 5-25°N, 45-95°E) presented by Kloss et al. (2019). The measurements showed that the main smoke layer (in terms of mean extinction coefficient for an area of 1000 km × 5000 km with center over India) ascended from approximately the tropopause at 16-17 km (10 September 2017) to about 20-21 km height (10 January 2018) and thus with an average speed of the order of 1000 m per month in the tropics.

4 Conclusions

The spread of extremely high amounts of wildfire smoke injected into the UTLS over western Canada in August 2017 and the decay of the stratospheric perturbation were monitored and documented with a network of 28 ground-based lidars in Europe. Stratospheric soot layers were observed for six months from August 2017 to January 2018. The AOT decreased from initial values of >0.2 (in the second half of August) to 0.005-0.03 in the beginning of September 2017 and then to around 0.003-0.004 during the following months until January 2018. Layer mean extinction coefficients and soot mass concentrations were of the order of 1 Mm^{-1} and 0.1 μg m^{-3} over the months, respectively, and thus significantly above the minimum stratospheric aerosol background values (0.1-0.2 Mm^{-1}, 0.01-0.02 μg m^{-3}). The decrease of the particle linear depolarization ratio with time was found to be consistent with the removal of the larger smoke particles and changes in the smoke particle shape properties (from non-spherical to spherical particle shape). The estimated ice-nucleating particle (INP) concentration levels were significantly enhanced for several months and thus the smoke plumes served as a long-lasting reservoir for INPs able to trigger heterogeneous ice nucleation and in this way to influence cirrus formation at tropopause level.

This record-breaking stratospheric smoke event is the second major event after the Eyjafjallajökull volcaninc eruption in 2010 (Ansmann et al., 2011; Pappalardo et al., 2013; Navas-Guzmán et al., 2013) that highlights the importance, need, and usefulness of EARLINET, a well-organized, Europe-wide, ground-based aerosol profiling network of advanced lidars. Dense sets of height and temporally resolved measurements of geometrical, optical, and microphysical smoke particle properties

5   were collected to document this event of a significant stratospheric perturbation in the northern hemisphere, to support aerosol transport and life cycle modeling with global atmospheric circulation models (Earth System Models, covering aerosol long-range transport, spread, and removal, and the influence of the aerosol layers on climate-relevant processes), and also to support spaceborne remote sensing of aerosols by providing high quality ground-truth data. The PollyNET observations have shown that automated, continuously running lidar systems are powerful tools and allow us to cover the decay phase of the stratospheric

10 aerosol perturbation in a coherent way. Without having continuous measurements, the smoke layering details and properties as presented and discussed in this article would widely remain undetected. At European level, an upgrade of the current lidar capabilities is foreseen in terms of aerosol observation in the implementation of ACTRIS as research infrastructure. In this framework it is aimed to move towards powerful and continuously running automated lidars.

The research on this spectacular case of a stratospheric perturbation is ongoing and will be widely based on spaceborne

15 active and passive remote sensing in combination with ground-based remote sensing (EARLINET and further ground-based lidar observations, e.g., in Asia and North America). This will then provide a good basis for sophisticated aerosol modeling. The complex transport features and climatic influences of stratospheric soot layers make it necessary to compare simulated smoke scenarios and the evolution of the smoke layer during long-range transport with the available observations. In this context one should finally mention (as an outlook what is left to be improved) that the realization of a well-organized ground-based

20 lidar network such as EARLINET, but on a hemispheric or even global scale (as the Global Aerosol Watch (GAW) initiative GALION: GAW Aerosol LIdar Observations Network) (Bösenberg et al., 2008) would be desirable and could be seen as big step forward towards a complete monitoring of global aerosol distributions and environmental conditions in the troposphere and stratosphere around the world. Sawamura et al. (2012) demonstrated the importance of having such a coordinated lidar profiling effort in the case of the Nabro volcanic eruption event. The importance for the need of such global aerosol monitoring

25 network structures may increase during the upcoming years because of the hypothesis that in a changing climate natural hazards such as severe wildfires combined with pyroCb activity and major desert dust outbreaks may occur more frequently and that detailed profile observations are required to support weather and climate research and forecast. Future activities should also be undertaken in the direction of harmonization of lidar observations and data. In this sense, the effort to develop standardized tools for aerosol lidar analysis, as realized in the case of ACTRIS/EARLINET in form of the single-calculus-chain (SCC)

30 software (D'Amico et al., 2015, 2016; Mattis et al., 2016), and to open its use to non-EARLINET lidar stations and teams is another step forward on the long way of global lidar data harmonization.

5 Data availability

EARLINET data are accessible through the ACTRIS data portal http://actris.nilu.no/. The long-term Polly lidar level-0 data are plotted online at polly.tropos.de, raw data are available at TROPOS upon request (polly@tropos.de). GDAS meteorological data can be downloaded at https://www.ready.noaa.gov/READYamet.php. GDAS1 data is available via the ARL webpage https://www.ready.noaa.gov/gdas1.php. All the analysis products are available at TROPOS upon request (info@tropos.de).

6 Author contributions

H.B. coordinated the project, communicated with all EARLINET groups and collected all EARLINET data. K.O. performed the Polly data analysis and prepared all figures supervised by H.B. and A.A. The layout of the manuscript was designed by A.A. and H.B. Finally, A.A. wrote the text in cooperation with H.B. and K.O. All EARLINET and further PollyNET co-authors performed the stratospheric smoke measurments, carefully analysed their observations with focus on stratospheric aerosol signatures and transfered the findings to TROPOS.

7 Competing interests

The authors declare that they have no conflict of interest.

Acknowledgements. The authors acknowledge support through ACTRIS under grant agreement no. 262 254 and BACCHUS (no. 603445) of the European Union Seventh Framework Programme (FP7/2007-2013), ACTRIS-2 and EXCELSIOR under grant agreement no. 654109 and 763643 from the European Union's Horizon 2020 research and innovation programme, and HD(CP)2 under grant agreement no. 01LK1502I by the German Ministry for Education and Research (BMBF). The research leading to these results has received funding also from the H2020 program of the European Union regarding GRASP-ACE (grant agreement no. 778349) and Spanish fundings (ref. TEC2015-63832-P, CGL2017-90884-REDT and MDM-2016-0600). Cork lidar observations were supported by the Irish Research Council (2014) and Science Foundation Ireland (05/RF/EEB011). Haifa lidar observations were funded by the German-Israeli Foundation (GIF grant I-1262 401.10/2014) with support of the Norman and Helen Asher Fund. The development of the lidar inversion algorithm used to analyze Lille and Leipzig lidar data was supported by the Russian Science Foundation (project 16-17-10241).

References

Althausen, D., Engelmann, R., Baars, H., Heese, B., Ansmann, A., Müller, D., and Komppula, M.: Portable Raman Lidar Polly­XT for Automated Profiling of Aerosol Backscatter, Extinction, and Depolarization, J. Atmos. Oceanic Tech., 26, 2366-2378, doi:10.1175/2009JTECHA1304.1, 2009.

5 Ansmann, A., Mattis, I., Wandinger, U., Wagner, F., Reichardt, J., and Deshler, T.: Evolution of the Pinatubo Aerosol: Raman Lidar Observa­tions of Particle Optical Depth, Effective Radius, Mass, and Surface Area over Central Europe at 53.48°N, J. Atmos. Sci., 54, 2630–2641, https://doi.org/10.1175/1520-0469(1997)054<2630:EOTPAR>2.0.CO;2, 1997.

Asmann, A., Tesche, M., Seifert P, Groß, S., Freudenthaler, V., Apituley, A., Wilson, K. M., Serikov, I., Linné, H., Heinold, B., Hiebsch, A., Schnell, F., Schmidt, J., Mattis, I., Wandinger, U., and Wiegner, M.: Ash and fine–mode particle mass profiles from EARLINET-

10 AERONET observations over central Europe after the eruptions of the Eyjafjallajökull volcano in 2010, J. Geophys. Res., 116, D00U02, doi:10.1029/2010JD015567, 2011.

Ansmann, A., Baars, H., Chudnovsky, A., Mattis, I., Veselovskii, I., Haarig, M., Seifert, P., Engelmann, R., and Wandinger, U.: Extreme levels of Canadian wildfire smoke in the stratosphere over central Europe on 21–22 August 2017, Atmos. Chem. Phys., 18, 11831-11845, https://doi.org/10.5194/acp-18-11831-2018, 2018.

15 Baars, H., Kanitz, T., Engelmann, R., Althausen, D., Heese, B., Komppula, M., Preißler, J., Tesche, M., Ansmann, A., Wandinger, U., Lim, J.-H., Ahn, J. Y., Stachlewska, I. S., Amiridis, V., Marinou, E., Seifert, P., Hofer, J., Skupin, A., Schneider, F., Bohlmann, S., Foth, A., Bley, S., Pfüller, A., Giannakaki, E., Lihavainen, H., Viisanen, Y., Hooda, R. K., Pereira, S. N., Bortoli, D., Wagner, F., Mattis, I., Janicka, L., Markowicz, K. M., Achtert, P., Artaxo, P., Pauliquevis, T., Souza, R. A. F., Sharma, V. P., van Zyl, P. G., Beukes, J. P., Sun, J., Rohwer, E. G., Deng, R., Mamouri, R.-E., and Zamorano, F.: An overview of the first decade of PollyNET: an emerging network of automated

20 Raman-polarization lidars for continuous aerosol profiling, Atmos. Chem. Phys., 16, 5111-5137, doi:10.5194/acp-16-5111-2016, 2016.

Boers, R., de Laat, A. T., Stein Zweers, D. C., and Dirksen, R. J.: Lifting potential of solar-heated aerosol layers, Geophys. Res. Lett., 37, L24802, doi:10.1029/2010GL045171, 2010.

Bösenberg, J, Hoff, R., Ansmann, A., Müller, D., Antuña-Marrero, J. C., Whiteman, D., Sugimoto, N., Apituley, A., Hardesty, M., Welton, E., Eloranta, E., Arshinov, Y., Kinne, S., and Freudenthaler, V.: Plan for the implementation of the GAW Aerosol Lidar Observation Network

25 GALION (Hamburg, Germany, 27-29 March 2007), WMO TD No. 1443, 52 pp, November 2008, 2008.

Butchart, N.: The Brewer-Dobson circulation, Rev. Geophys., 52, 157-184, doi:10.1002/2013RG000448, 2014.

Cheremisin, A. A., Vassilyev, Y. V., and Horvath, H.: Gravito-photophoresis and aerosol stratification in the atmosphere, J. Aerosol. Sci., 36, 1277–1299, doi:10.1016/j.jaerosci.2005.02.003, 2005.

Cheremisin, A. A., Shnipov, I. S., Horvath, H., and Rohatschek, H.: The global picture of aerosol layers formation in the stratosphere

30 and in the mesosphere under the influence of gravito-photophoretic and magneto-photophoretic forces, J. Geophys. Res., 116, D19204, doi:10.1029/2011JD015958, 2011.

Dahlkötter, F., Gysel, M., Sauer, D., Minikin, A., Baumann, R., Seifert, P., Ansmann, A., Fromm, M., Voigt, C., and Weinzierl, B.: The Pagami Creek smoke plume after long-range transport to the upper troposphere over Europe – aerosol properties and black carbon mixing state, Atmos. Chem. Phys., 14, 6111–6137, https://doi.org/10.5194/acp-14-6111-2014, 2014.

35 D'Amico, G., Amodeo, A., Baars, H., Binietoglou, I., Freudenthaler, V., Mattis, I., Wandinger, U., and Pappalardo, G.: EARLINET Single Calculus Chain - overview on methodology and strategy, Atmos. Meas. Tech., 8, 4891-4916, https://doi.org/10.5194/amt-8-4891-2015, 2015.

D'Amico, G., Amodeo, A., Mattis, I., Freudenthaler, V., and Pappalardo, G.: EARLINET Single Calculus Chain - technical - Part 1: Pre-processing of raw lidar data, Atmos. Meas. Tech., 9, 491-507, https://doi.org/10.5194/amt-9-491-2016, 2016.

de Laat, A. T. J., Stein Zweers, D. C., Boers, R., and Tuinder, O. N. E.: A solar escalator: Observational evidence of the self-lifting of smoke and aerosols by absorption of solar radiation in the February 2009 Australian Black Saturday plume, J. Geophys. Res., 117, D04204, doi:10.1029/2011JD017016, 2012.

Ditas, J., Ma, N., Zhang, Y., Assmann, D., Neumaier, M., Riede, H., Karu, E., Williams, J., Scharffe, D., Wang, Q., Saturno, J., Schwarz, J. P., Katich, J. M., McMeeking, G. R., Zahn, A., Hermann, M., Brenninkmeijer, C. A. M., Andreae, M. O., Pöschl, U., Su, H., and Cheng, Y.: Strong impact of wildfires on the abundance and aging of black carbon in the lowermost stratosphere, Proceedings of the National Academy of Sciences, 115, E11595-E11603, doi: 10.1073/pnas.1806868115, 2018.

EARLINET data base, available at: ACTRIS data portal, http://actris.nilu.no/, last access: 20 May, 2019.

Engelmann, R., Kanitz, T., Baars, H., Heese, B., Althausen, D., Skupin, A., Wandinger, U., Komppula, M., Stachlewska, I. S., Amiridis, V., Marinou, E., Mattis, I., Linné, H., and Ansmann, A.: The automated multiwavelength Raman polarization and water-vapor lidar PollyXT: the neXT generation, Atmos. Meas. Tech., 9, 1767-1784, doi:10.5194/amt-9-1767-2016, 2016.

Finger, F.: Aerosolschichten in der oberen Troposphäre und unteren Stratosphäre über Mitteleuropa, University Master Thesis, 89 pages, Universität Leipzig, Germany, 2011.

Forestieri, S. D., Helgestad, T. M., Lambe, A. T., Renbaum-Wolff, L., Lack, D. A., Massoli, P., Cross, E. S., Dubey, M. K., Mazzoleni, C., Olfert, J. S., Sedlacek III, A. J., Freedman, A., Davidovits, P., Onasch, T. B., and Cappa, C. D.: Measurement and modeling of the multiwavelength optical properties of uncoated flame-generated soot, Atmos. Chem. Phys., 18, 12141-12159, https://doi.org/10.5194/acp-18-12141-2018, 2018.

Freudenthaler, V.: About the effects of polarising optics on lidar signals and the $\Delta 90$ calibration, Atmos. Meas. Tech., 9, 4181-4255, https://doi.org/10.5194/amt-9-4181-2016, 2016.

Fromm, M., Alfred, J., Hoppel, K., Hornstein, J., Bevilacqua, R., Shettle, E., Servranckx, R., Li, Z., Stocks, B.: Observations of boreal forest fire smoke in the stratosphere by POAM III, SAGE II, and lidar in 1998, Geophys. Res. Lett., 27, 1407–1410, 2000.

Fromm, M. D., and Servranckx, R.: Transport of forest fire smoke above the tropopause by supercell convection, Geophys. Res. Lett., 30, 1542, doi:10.1029/2002GL016820, 2003.

Fromm, M., Shettle, E. P., Fricke, K. H., Ritter, C., Trickl, T., Giehl, H., Gerding, M., Barnes, J. E., O'Neill, M., Massie, S. T., Blum, U., McDermid, I. S., Leblanc, T., and Deshler, T.: Stratospheric impact of the Chisholm pyrocumulonimbus eruption: 2. Vertical profile perspective, J. Geophys. Res., 113, D08203, doi:10.1029/2007JD009147, 2008.

Fromm, M., Lindsey, D. T., Servranckx, R., Yue, G., Trickl, T., Sica, R., Doucet, P., and Godin-Beekmann, S. E.: The untold story of pyrocumulonimbus, B. Am. Meteorol. Soc., 91, 1193–1209, doi:10.1175/2010bams3004.1, 2010.

GDAS: Global Data Assimilation System, meteorological data base, available at: https://www.ready.noaa.gov/gdas1.php, last access: 20 May, 2019.

Gialitaki, A., Amiridis, V., Tsikeri, A., Haarig, M., Baars, H., and Ansmann, A.: Is the near-spherical shape the 'new black' for smoke?, Atmos. Chem. Phys., to be submitted to speicla issue of EARLINET, 2019.

Haarig, M., Ansmann, A., Baars, H., Jimenez, C., Veselovskii, I., Engelmann, R., and Althausen, D.: Depolarization and lidar ratios at 355, 532, and 1064 nm and microphysical properties of aged tropospheric and stratospheric Canadian wildfire smoke, Atmos. Chem. Phys., 18, 11847-11861, https://doi.org/10.5194/acp-18-11847-2018, 2018.

Hoose, C. and Möhler, O.: Heterogeneous ice nucleation on atmospheric aerosols: a review of results from laboratory experiments, Atmos. Chem. Phys., 12, 9817-9854, https://doi.org/10.5194/acp-12-9817-2012, 2012.

Hu, Q., Goloub, P., Veselovskii, I., Bravo-Aranda, J.-A., Popovici, I. E., Podvin, T., Haeffelin, M., Lopatin, A., Dubovik, O., Pietras, C., Huang, X., Torres, B., and Chen, C.: Long-range-transported Canadian smoke plumes in the lower stratosphere over northern France, Atmos. Chem. Phys., 19, 1173-1193, https://doi.org/10.5194/acp-19-1173-2019, 2019.

Jensen, E. J., and Toon, O. B.: The potential effects of volcanic aerosols on cirrus cloud microphysics, Geophys. Res. Lett., 19, 1759–1762, http://dx.doi.org/10.1029/92GL01936, 1992.

Jimenez, C., Ansmann, A., Engelmann, R., Haarig, M., Schmidt, J., and Wandinger, U.: Polarization lidar: an extended three-signal calibration approach, Atmos. Meas. Tech., 12, 1077-1093, https://doi.org/10.5194/amt-12-1077-2019, 2019.

Kanji, Z. A., Ladino, L. A., Wex, H., Boose, Y., Burkert-Kohn, M., Cziczo, D. J., and Krämer, M.: Chapter 1: Overview of ice nucleating particles, Meteor Monogr., Am. Meteorol. Soc., 58, 1.1-1.33, https://doi.org/10.1175/amsmonographs-d-16-0006.1, 2017.

Kar, J., Lee, K.-P., Vaughan, M. A., Tackett, J. L., Trepte, C. R., Winker, D. M., Lucker, P. L., and Getzewich, B. J.: CALIPSO Level 3 Stratospheric Aerosol Product: Version 1.00 Algorithm Description and Initial Assessment, Atmos. Meas. Tech. Discuss., https://doi.org/10.5194/amt-2019-245, in review, 2019.

Khaykin, S. M., Godin-Beekmann, S., Hauchecorne, A., Pelon, J., Ravetta, F., and Keckut, P.: Stratospheric smoke with unprecedentedly high backscatter observed by lidars above southern France, Geophys. Res. Lett., 45, https://doi.org/10.1002/2017GL076763, 2018.

Kloss, C., Berthet, G., Sellitto, P., Ploeger, F., Bucci, S., Khaykin, S., Jègou, F., Taha, G., Thomason, L. W., Barret, B., Le Flochmoen, E., von Hobe, M., Bossolasco, A., Bègue, N., and Legras, B.: Transport of the 2017 Canadian wildfire plume to the tropics and global stratosphere via the Asian monsoon circulation, Atmos. Chem. Phys. Discuss., https://doi.org/10.5194/acp-2019-204, in review, 2019.

Liu, X., and Penner, J. E.: Effect of Mount Pinatubo H2SO4/H2O aerosol on ice nucleation in the upper troposphere using a global chemistry and transport model, J. Geophys. Res., 107(D12), doi:10.1029/2001JD000455, 2002.

Mamouri, R. E. and Ansmann, A.: Fine and coarse dust separation with polarization lidar, Atmos. Meas. Tech., 7, 3717-3735, https://doi.org/10.5194/amt-7-3717-2014, 2014.

Mamouri, R.-E. and Ansmann, A.: Potential of polarization lidar to provide profiles of CCN- and INP-relevant aerosol parameters, Atmos. Chem. Phys., 16, 5905-5931, doi:10.5194/acp-16-5905-2016, 2016.

Mamouri, R.-E. and Ansmann, A.: Potential of polarization/Raman lidar to separate fine dust, coarse dust, maritime, and anthropogenic aerosol profiles, Atmos. Meas. Tech., 10, 3403-3427, https://doi.org/10.5194/amt-10-3403-2017, 2017.

Mattis, I., Seifert, P., Müller, D., Tesche, M., Hiebsch, A., Kanitz, T., Schmidt, J., Finger, F., Wandinger, U., and Ansmann, A.: Volcanic aerosol layers observed with multiwavelength Raman lidar over central Europe in 2008-–2009, J. Geophys. Res., 115, D00L04, doi:10.1029/2009JD013472, 2010.

Mattis, I., D'Amico, G., Baars, H., Amodeo, A., Madonna, F., and Iarlori, M.: EARLINET Single Calculus Chain – technical – Part 2: Calculation of optical products, Atmos. Meas. Tech., 9, 3009-3029, https://doi.org/10.5194/amt-9-3009-2016, 2016.

Navas-Guzmán, F., Müller, D., Bravo-Aranda, J. A., Guerrero-Rascado, J. L., Granados-Muñoz, M. J., Pérez-Ramírez, D., Olmo,, F. J. and Alados-Arboledas, L.: Eruption of the Eyjafjallajökull Volcano in spring 2010: Multiwavelength Raman lidar measurements of sulphate particles in the lower troposphere, J. Geophys. Res. Atmos., 118, 1804– 1813, doi:10.1002/jgrd.50116, 2013.

Pappalardo, G., Mona, L., D'Amico, G., Wandinger, U., Adam, M., Amodeo, A., Ansmann, A., Apituley, A., Alados Arboledas, L., Balis, D., Boselli, A., Bravo-Aranda, J. A., Chaikovsky, A., Comeron, A., Cuesta, J., De Tomasi, F., Freudenthaler, V., Gausa, M., Giannakaki, E., Giehl, H., Giunta, A., Grigorov, I., Groß, S., Haeffelin, M., Hiebsch, A., Iarlori, M., Lange, D., Linné, H., Madonna, F., Mattis, I.,

Mamouri, R.-E., McAuliffe, M. A. P., Mitev, V., Molero, F., Navas-Guzman, F., Nicolae, D., Papayannis, A., Perrone, M. R., Pietras, C., Pietruczuk, A., Pisani, G., Preißler, J., Pujadas, M., Rizi, V., Ruth, A. A., Schmidt, J., Schnell, F., Seifert, P., Serikov, I., Sicard, M., Simeonov, V., Spinelli, N., Stebel, K., Tesche, M., Trickl, T., Wang, X., Wagner, F., Wiegner, M., and Wilson, K. M.: Four-dimensional distribution of the 2010 Eyjafjallajökull volcanic cloud over Europe observed by EARLINET, Atmos. Chem. Phys., 13, 4429-4450, https://doi.org/10.5194/acp-13-4429-2013, 2013.

Pappalardo, G., Amodeo, A., Apituley, A., Comeron, A., Freudenthaler, V., Linné, H., Ansmann, A., Bösenberg, J., D'Amico, G., Mattis, I., Mona, L., Wandinger, U., Amiridis, V., Alados-Arboledas, L., Nicolae, D., and Wiegner, M.: EARLINET: towards an advanced sustainable European aerosol lidar network, Atmos. Meas. Tech., 7, 2389–2409, doi:10.5194/amt-7-2389-2014, 2014.

Peterson, D. A., Hyer, E. J., Campbell, J. R., Solbrig, J. E., and Fromm, M. D.: A conceptual model for development of intense pyrocumulonimbus in western North America, Mon. Wea. Rev., 145, 2235–2255, doi.org/10.1175/MWR-D-16-0232.1, 2017.

Peterson, D. A., Campbell, J. R., Hyer, E. J., Fromm, M. D., Kablick III, G. P., Cossuth, J. H., and DeLand, M. T.: Wildfire-driven thunderstorms cause a volcano-like stratospheric injection of smoke, npj Climate and Atmospheric Science, 1, article number 30, https://doi.org/10.1038/s41612-018-0039-3, 2018.

Pueschel, R. F., Verma, S., Rohatschek, H., Ferry, G. V., Boiadjieva, N., Howard, S. D., and Strawa, A. W.: Vertical transport of anthropogenic soot aerosol into the middle atmosphere, J. Geophys. Res., 105, 3727–3736, doi:10.1029/1999JD900505, 2000.

Renard, J.-B., Brogniez, C., Berthet, G., Bourgeois, Q., Gaubicher, B., Chartier, M., Balois, J.-Y., Verwaerde, C., Auriol, F., Francois, P., Daugeron, D., and Engrand, C.: Vertical distribution of the different types of aerosols in the stratosphere: Detection of solid particles and analysis of their spatial variability, J. Geophys. Res., 113, D21303, doi:10.1029/2008JD010150, 2008.

Rissler, J., Messing, M. E., Malik, A. I., Nilsson, P. T., Nordin, E. Z., Bohgard, M., Sanati, M., and Pagels, J. H.: Effective density characterization of soot agglomerates from various sources and comparison to aggregation theory, Aerosol Sci. Technol., 47, 792–805, doi:10.1080/02786826.2013.7913, 2013.

Rohatschek, H.: Levitation of stratospheric and mesospheric aerosols by gravito-photophoresis, J. Aerosol. Sci., 27, 467–475, 1996.

Rosenfeld, D., Fromm, M., Trentmann, J., Luderer, G., Andreae, M. O., and Servranckx, R.: The Chisholm firestorm: observed microstructure, precipitation and lightning activity of a pyro-cumulonimbus, Atmos. Chem. Phys., 7, 645-659, https://doi.org/10.5194/acp-7-645-2007, 2007.

Sassen, K., Starr, D. O. C. , Mace, G. G., Poellot, M. R., Melfi, S. H., Eberhard, W. L., Spinhirne, J. D., Eloranta, E. W., Hagen, D. E., and Hallett, J.: The 5-6 December 1991 FIRE IFO II jet stream cirrus case study: Possible influences of volcanic aerosols, J. Atmos. Sci., 52, 97-123, 1995.

Sawamura, P., Vernier, J. P., Barnes, J. E., Berkoff, T. A. Welton, E. J., Alados-Arboledas, L., Navas-Guzmán, F., Pappalardo, G., Mona, L., Madonna, F., Lange, D., Sicard, M., Godin-Beekmann, S., Payen, G., Wang, Z., Hu, S., Tripathi, S. N., Cordoba-Jabonero, C., and Hoff, R. M.: Stratospheric AOD after the 2011 eruption of Nabro volcano measured by lidars over the Northern Hemisphere, Environ. Res. Lett.7, 034013 (9pp), doi:10.1088/1748-9326/7/3/034013, 2012.

Seviour, W. J. M., Butchart, N. and Hardiman, S. C.: The Brewer– Dobson circulation inferred from ERA-Interim, Q.J.R. Meteorol. Soc., 138, 878– 888, doi: 10.1002/qj.966, 2012.

Siddaway, J. M., and Petelina, S. V.: Transport and evolution of the 2009 Australian Black Saturday bushfire smoke in the lower stratosphere observed by OSIRIS on Odin, J. Geophys. Res., 116, D06203, doi: 10.1029/2010JD015162, 2011.

Sicard, M., Granados-Muñoz, M. J., Alados-Arboledas, L., Barragán, R., Bedoya-Velásquez, A. E., Benavent-Oltra, J. A., Bortoli, D., Comerón, A., Córdoba-Jabonero, C., Costa, M. J., del Águila, A., Fernández, A. J., Guerrero-Rascado, J. L., Jorba, O., Molero, F.,

Muñoz-Porcar, C., Ortiz-Amezcua, P., Papagiannopoulos, N., Potes, M., Pujadas, M., Rocadenbosch, F., Rodríguez-Gómez, A., Román, R., Salgado, R., Salgueiro, V., Sola, Y., and Yela, M.: Ground/space, passive/active remote sensing observations coupled with particle dispersion modelling to understand the inter-continental transport of wildfire smoke plumes, Remote Sensing of the Environment, 232, https://doi.org/10.1016/j.rse.2019.111294, 2019.

5   Smith, A. J. A., Peters, D. M., McPheat, R., Lukanihins, S., and Grainger, R. G.: Measuring black carbon spectral extinction in the visible and infrared, J. Geophys. Res. Atmos., 120, 9670–9683, doi:10.1002/2015JD023564, 2015.

Trickl, T., Giehl, H., Jäger, H., and Vogelmann, H.: 35 yr of stratospheric aerosol measurements at Garmisch-Partenkirchen: from Fuego to Eyjafjallajökull, and beyond, Atmos. Chem. Phys., 13, 5205-5225, https://doi.org/10.5194/acp-13-5205-2013, 2013.

Trickl, T., Vogelmann, H., Giehl, H., Scheel, H.-E., Sprenger, M., and Stohl, A.: How stratospheric are deep stratospheric intrusions?, Atmos.
10   Chem. Phys., 14, 9941-9961, https://doi.org/10.5194/acp-14-9941-2014, 2014.

Trickl, T., Vogelmann, H., Fix, A., Schäfler, A., Wirth, M., Calpini, B., Levrat, G., Romanens, G., Apituley, A., Wilson, K. M., Begbie, R., Reichardt, J., Vömel, H., and Sprenger, M.: How stratospheric are deep stratospheric intrusions? LUAMI 2008, Atmos. Chem. Phys., 16, 8791-8815, https://doi.org/10.5194/acp-16-8791-2016, 2016.

Ullrich, R., Hoose, C., Möhler, O., Niemand, M., Wagner, R., Höhler, K., Hiranuma, N., Saathoff, H., and Leisner, T.: A new ice nucleation
15   active site parameterization for desert dust and soot, J. Atmos. Sci., 74, 699–717, doi: 10.1175/JAS-D-16-0074.1, 2017.

Vernier, J., Fairlie, T.D., Deshler, T., Venkat Ratnam, M., Gadhavi, H., Kumar, B. S., Natarajan, M., Pandit, A. K., Akhil Raj, S. T., Hemanth Kumar, A., Jayaraman, A., Singh, A. K., Rastogi, N., Sinha, P. R., Kumar, S., Tiwari, S., Wegner, T., Baker, N., Vignelles, D., Stenchikov, G., Shevchenko, I., Smith, J., Bedka, K., Kesarkar, A., Singh, V., Bhate, J., Ravikiran, V., Durga Rao, M., Ravindrababu, S., Patel, A., Vernier, H., Wienhold, F. G., Liu, H., Knepp, T. N., Thomason, L., Crawford, J., Ziemba, L., Moore, J., Crumeyrolle, S., Williamson,
20   M., Berthet, G., Jegou, F., and Renard, J.: BATAL: The Balloon Measurement Campaigns of the Asian Tropopause Aerosol Layer, Bull. Amer. Meteor. Soc., 99, 955–973, https://doi.org/10.1175/BAMS-D-17-0014.1, 2018.

Zuev, V. V., Gerasimov, V. V., Nevzorov, A. V., and Savelieva, E. S.: Lidar observations of pyrocumulonimbus smoke plumes in the UTLS over Tomsk (Western Siberia, Russia) from 2000 to 2017, Atmos. Chem. Phys., 19, 3341-3356, https://doi.org/10.5194/acp-19-3341-2019, 2019.

Table 1. Lidar-derived smoke (soot) particle optical and microphysical properties and retrieval input parameters for 532 nm. z_{bot} and z_{top} are the layer base and top height of the detected stratospheric smoke layer, respectively. The values for the lidar ratio S_p and the two conversion factors c_v and c_s are taken from Haarig et al. (2018) and the estimate of particle density density ρ_p is based on Rissler et al. (2013). For detailed explanations see text.

Parameter	Symbol	Value
Backscatter coefficient	β_p	
Integrated backscatter coefficient	$B_{\Pi,p} = \int_{z_{bot}}^{z_{top}} \beta_p dz$	
Extinction coefficient	$\sigma_p = S_p \beta_p$	
Lidar ratio	S_p	65 sr
Aerosol optical thickness (AOT)	$\tau_p = \int_{z_{bot}}^{z_{top}} \sigma_p dz$	
Mass concentration	$M_p = \rho_p c_v \sigma_p = \sigma_p / k_{ext}$	
Particle density	ρ_p	0.9 g cm^{-3}
Extinction-to-volume conversion factor	c_v	0.1244×10^{-6} Mm m^3 m^{-3}
Mass-specific extinction coefficient	$k_{ext} = 1/(\rho_p c_v)$	8.93 m^2 g^{-1}
Surface area concentration	$s_p = c_s \sigma_p$	
Extinction-to-surface conversion factor	c_s	1.166×10^{-12} Mm m^2 m^{-3}
Ice-nucleating particle concentration	$n_{INP} = s_p \eta_{dep}(T, S_{ice})$	
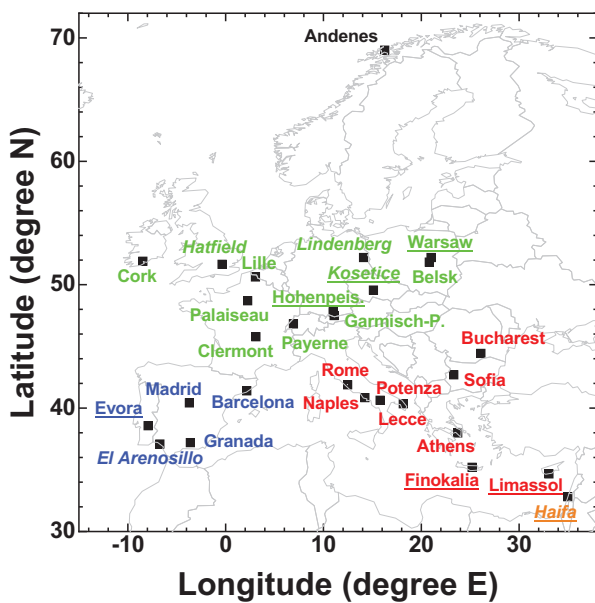
Figure 1. Lidar network of 23 ACTRIS/EARLINET stations and 5 non-EARLINET sites (in italics). This network observed stratospheric smoke layers from August 2017 to January 2018. Northern (black), central and western (green), southwestern (blue), southeastern European (red), and Israel (orange) lidar sites are distinguished. Polly stations are underlined.
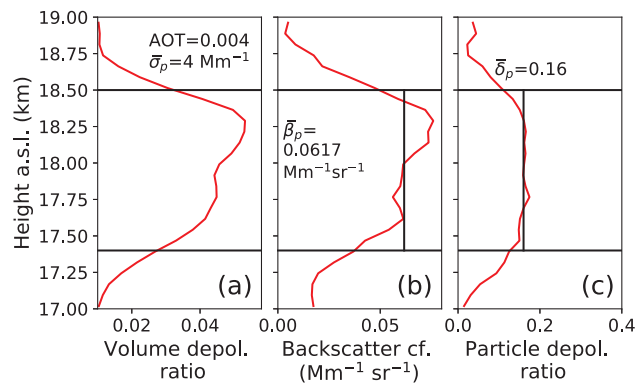
Figure 2. Analysis of a Polly measurement at Limassol, Cyprus, on 9 September 2017. The shown 532 nm backscatter and depolarization ratio profiles are computed from six-hour mean lidar return signal profiles (18:00-24:00 UTC). Vertical signal smoothing with a window length of 367.5 m is applied. The volume depolarization ratio in (a) and the particle backscatter coefficient in (b) were used to identify the smoke layer. The shown smoke layer base and top heights (horizontal lines) are mean values for the observation period, estimated from subsequent 60-90-minute mean depolarization ratio profiles. The particle depolarization ratio in (c) is the one for smoke (after the correction for Rayleigh depolarization contributions). Values for the vertically mean particle extinction coefficient $\overline{\sigma_{\mathrm{p}}}$ (for the column from z_{bot} and z_{top}, assuming a lidar ratio of 65 sr) and 532 nm AOT, mean backscatter coefficient $\overline{\beta_{\mathrm{p}}}$, and mean particle linear depolarization ratio $\overline{\delta_{\mathrm{p}}}$ are stated in the three panels, respectively.
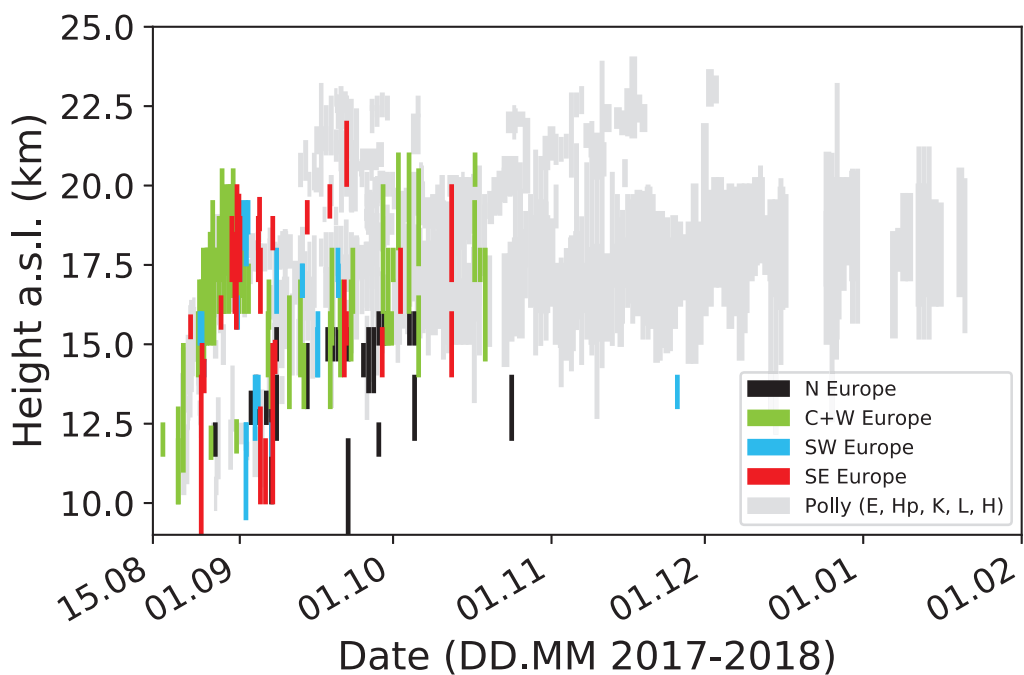
Figure 3. Overview of the lidar network observations of stratospheric smoke from August 2017 to January 2018. Each observation is considered as one colored vertical line indicating the vertical extent from layer base to top (in height above sea level, a.s.l.). One observation per day and site is considered. The colors separate the different European regions of the EARLINET stations as defined in Fig. 1. Polly observations (collected at Evora, Hohenpeissenberg, Kosetice, Limassol, and Haifa) are given here as grey background and are presented in Fig. 4.
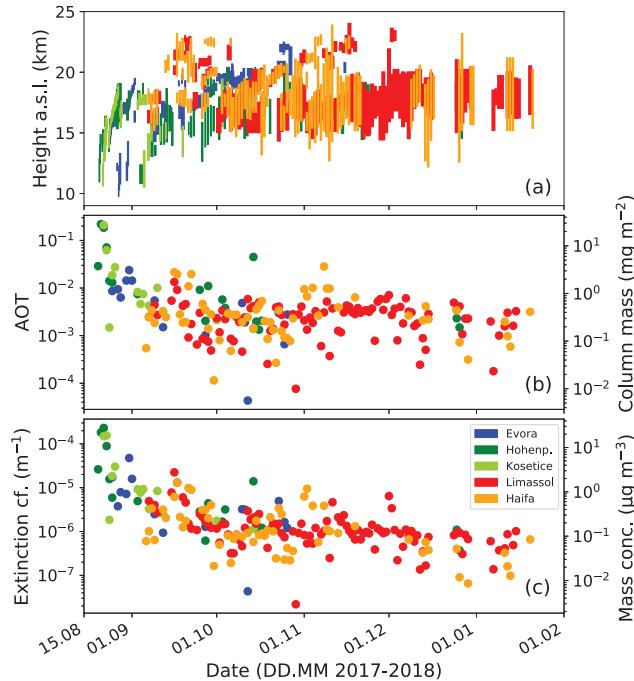
Figure 4. (a) Overview of all Polly observations of the stratospheric smoke layer (from base to top as colored vertical lines) performed at Evora, Portugal (blue), Hohenpeissenberg, Germany (olive), Kosetice, Czech Republik (green), Limassol, Cyprus (red), and Haifa, Israel (orange). For each station, one nighttime observation per day is considered. (b) Corresponding smoke layer AOT at 532 nm and estimated column-integrated smoke particle mass concentration, and (c) vertically mean smoke particle extinction coefficient and corresponding mean particle mass concentration.
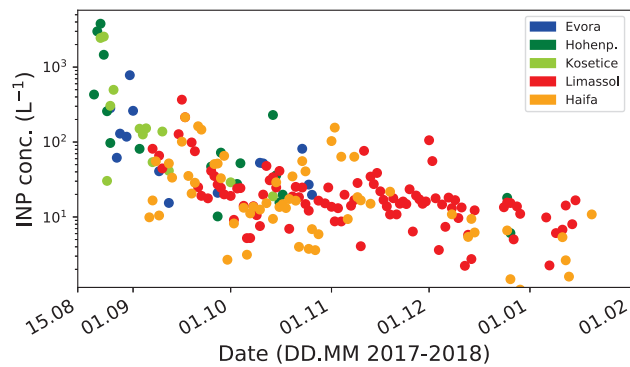
Figure 5. Ice-nucleating particle (INP) concentration estimated from the smoke extinction coefficients in Fig. 4(c), assuming heterogeneous ice nucleation (deposition nucleation) on soot particles at the temperature $T = -55°C$ and a typical ice supersaturation level during cirrus formation of S_{ice}=1.15 (Ullrich et al., 2017).
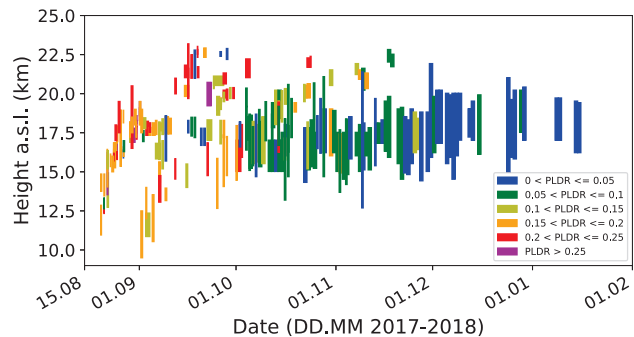
Figure 6. All individual day-by-day smoke observations of the 532 nm particle linear depolarization ratio (from all contributing stations, including several Lindenberg observations at 355 nm). Colors indicate different depolarization value ranges. The depolarization ratio decreased with time because of the removal of the larger non-spherical smoke particles and/or the change in the shape characteristics (from non-spherical to spherical particle shape).
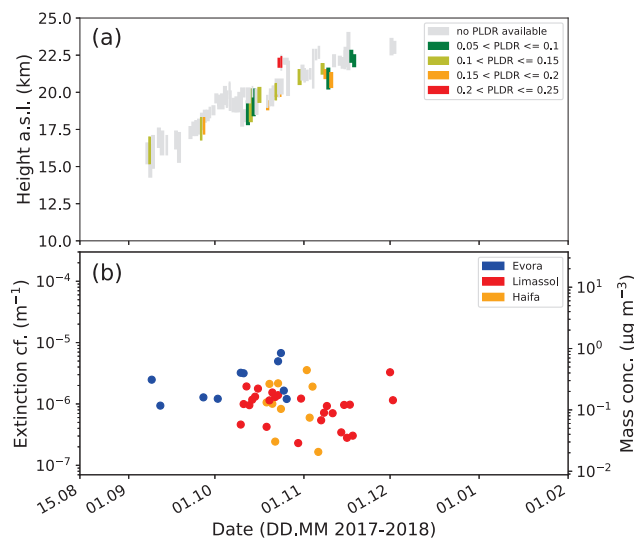
Figure 7. (a) Lidar observations of an apparently ascending smoke layer based on Polly observations at Evora, Limassol, and Haifa. Smoke layer base to top is shown as vertical line. Available layer mean linear depolarization ratios are highlighted as colored vertical lines, from green for low depolarization ratios to red for high depolarization ratios. (b) Corresponding vertically mean particle extinction coefficient and converted smoke mass concentration.
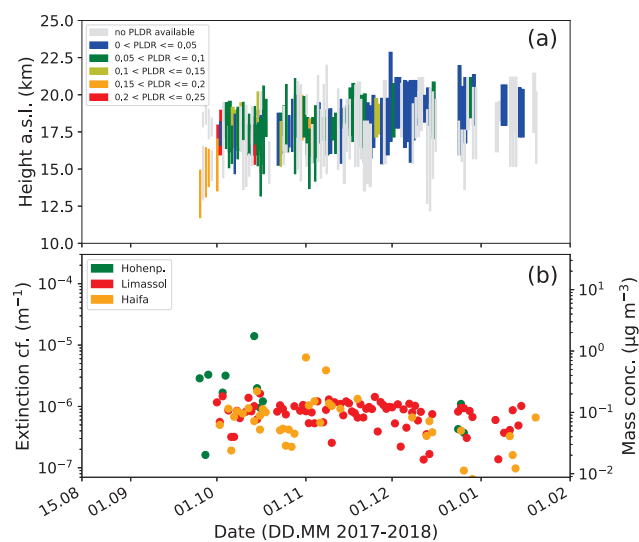
Figure 8. Same as Fig. 7, except for the main smoke layer (after removal of the ascending layer feature).
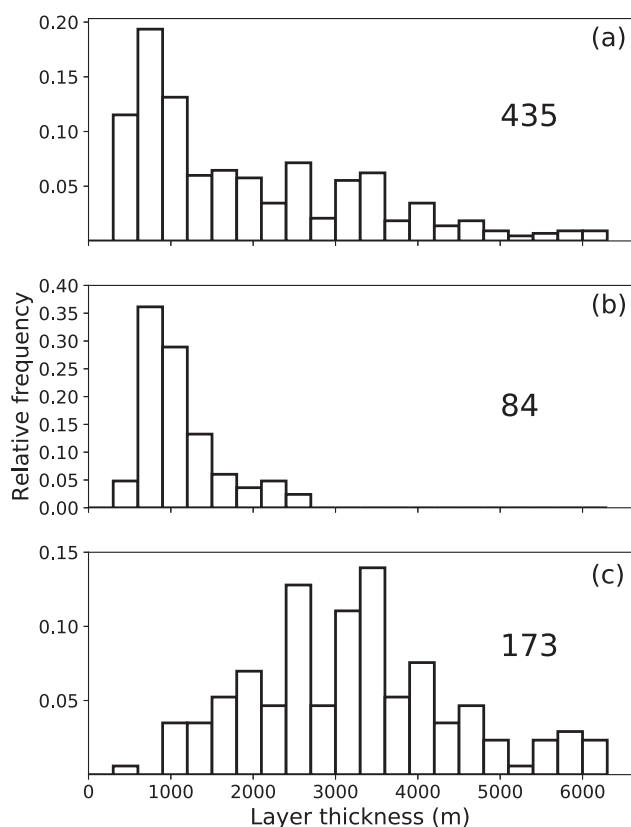
Figure 9. Frequency of occurrence (in all three panels) of day-by-day smoke layer depth considering (a) all 435 Polly observations in Fig. 4 from August 2017 to January 2018, (b) considering the 84 observations of the ascending layer (Fig. 7, from September to the beginning of December), and (c) the 173 measurements of the main layer (Fig. 8, from September 2017 to the end of January 2018).